Polarization of the RF Field in a Human Head at High Field: A Study With a Quadrature Surface Coil at 7.0 T

Jinghua Wang,[1] Qing X. Yang,[1]* Xiaoliang Zhang,[2] Christopher M. Collins,[1] Michael B. Smith,[1] Xiao-Hong Zhu,[2] Gregor Adriany,[2] Kamil Ugurbil,[2] and Wei Chen[2]

The RF field intensity distribution in the human brain becomes inhomogeneous due to wave behavior at high field. This is further complicated by the spatial distribution of RF field polarization that must be considered to predict image intensity distribution. An additional layer of complexity is involved when a quadrature coil is used for transmission and reception. To study such complicated RF field behavior, a computer modeling method was employed to investigate the RF field of a quadrature surface coil at 300 MHz. Theoretical and experimental results for a phantom and the human head at 7.0 T are presented. The results are theoretically important and practically useful for high-field quadrature coil design and application. Magn Reson Med 48:362–369, 2002. © 2002 Wiley-Liss, Inc.

Key words: computer modeling; high field MRI; RF field polarization; RF coil

The rapid increase in the number of high-field whole-body MRI systems (3.0–8.0 T) in recent years has resulted in a great deal of interest in RF field and coil engineering in the corresponding high-frequency regime (1–6). Coil construction for human-sized samples becomes increasingly difficult at high frequency (7). Furthermore, the image intensity distribution acquired at high field from human and water samples exhibits significant inhomogeneity (8–10). The most well-known example of such inhomogeneity is the conspicuous "bright spot" located approximately in the center of a head image acquired with a volume coil at field strengths of 4.0 T or above (10). This phenomenon has been attributed to the B_1 field wave behavior as the wavelength of this field approximates the dimension of the human-sized sample. Under such a condition, the phase of the RF field is a function of position inside the sample. As a result, the distributions of both magnitude and polarization of the RF field in the human samples are substantially different from the unloaded case and vary significantly with the electric properties and geometry of the sample. To design RF coils suitable for high-field applications, it is necessary to carefully examine the RF field polarization distribution with respect to electric properties and size of the human head or other sample of interest (8,11–14). The image intensity distribution of the samples with a given RF coil can be predicted from the calculated RF field distribution using its circularly polarized components (8,12–14). In the quasistatic frequency regime, the difference in the relative spatial distribution between the B_1 field magnitude and its polarized components is insignificant. The magnitude of the transverse B_1 field can be used directly to assess the signal intensity distribution. However, with a "linear" (single-channel) transmit/receive surface coil at 7.0 T, the distributions of the transverse B_1 field magnitude and its circularly polarized components are markedly different and only the latter can be used to reproduce the intensity variation seen in experimental images (12,14). This demonstrates that the polarization behavior of the RF field plays an important part in the formation of the image intensity distribution in a human sample at high field. An immediate question is how the B_1 field polarization behaves in a human sample with a quadrature coil. The motivation of using a quadrature RF coil is to produce a circularly polarized field in order to increase the image SNR and reduce RF transmission power (15–18). These advantages of quadrature excitation and reception are often used in MR experiments and clinical applications (19–21). Thus, it is important to understand the B_1 field polarization as it contributes to the final signal intensity distribution. From an engineering point of view, it is necessary to establish a computational tool that is capable of predicting the signal intensity distribution from a given sample–coil configuration. In this article, we present a detailed description of the computer-aided analytical method and the results of our investigation on the polarization behavior of the B_1 field at 300 MHz using a quadrature surface coil. The computer modeling method was validated by experimental results at 7.0 T. The effect of the electric properties of the sample on the polarization of the RF field is also investigated. These studies are not only practically useful for high-field quadrature coil designs and applications, but they also serve as a stepping stone for more complicated multicoil systems widely used for parallel acquisition techniques (22–24).

METHODS

Sample-Coil System and the Corresponding Computer Models

A shielded quadrature surface coil as shown in Fig. 1 was used for both transmission and reception. Each component of the coil consisted of a 14 × 11 cm rectangle built from copper foil with eight ceramic chip capacitors of 12 pF (American Technical Ceramics, New York, NY) placed equidistantly. The shield was connected to the RF coil ground. The distances from the shield to the coil and the

[1]Center for NMR Research, Department of Radiology, Pennsylvania State University College of Medicine, Hershey, Pennsylvania.

[2]Center for MR Research, Department of Radiology, School of Medicine, University of Minnesota, Minneapolis, Minnesota.

Grant sponsor: Whitaker Foundation; Grant number: RG-99-0157; Grant sponsor: NIH; Grant numbers: NS38070; NS39043; P41 RR08079; NS41262; Grant sponsors: Keck Foundation; MIND Institute; US Department of Energy.

*Correspondence to: Qing X. Yang, Center for NMR Research, NMR/MRI Building, Department of Radiology H066, The Pennsylvania State University College of Medicine, 500 University Drive, Hershey, PA 17033. E-mail: qyang@psu.edu

Received 31 January 2002; revised 1 March 2002; accepted 4 March 2002.
DOI 10.1002/mrm.10197
Published online in Wiley InterScience (www.interscience.wiley.com).

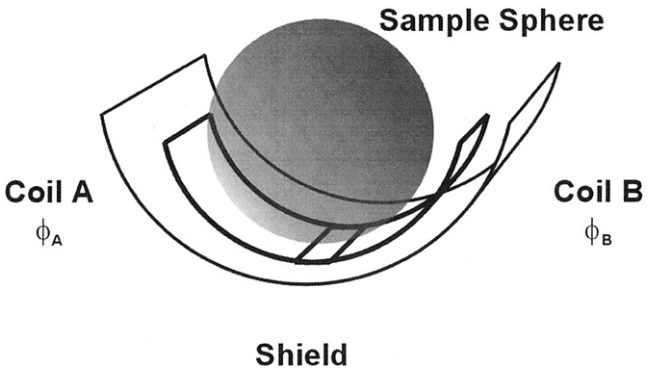

FIG. 1. A 3D picture of the surface quadrature coil and experimental setup. Coils A and B are driven by voltage sources with phases ϕ_A and ϕ_B, respectively. The quadrature coil is shielded with a continuous copper foil conformed to a semicylindrical surface 4 cm outside the coil.

coil to the sample were 4 and 2 cm, respectively. The computer model for phantom samples was built following the exact experimental configuration on a rectilinear grid with 2 mm resolution and total grid points of 160 × 160 × 120 in the x, y, and z dimensions. In the model, the coil was driven by sinusoidal voltage sources placed across all capacitors and driven at 300 MHz with appropriate phases. This method of modeling loaded RF coils and resultant fields for MRI has been proven accurate with experimental verification up to 128 MHz for a birdcage coil loaded with water, saline, and the human head (25), and up to 300 MHz for a linear surface coil loaded with saline and the human head (12,14).

The phantom consists of a 16-cm diameter spherical bottle filled with 20 mM NaCl. The phantom was modeled with an identical geometry, a relative permittivity (ϵ_r) of 78 and conductivity (σ) of 0.26 S/m. The conductivity of this phantom is about halfway between those of white matter and fat at 300 MHz. It was used because it produced a characteristic image intensity distribution at 7.0 T. The specific image distribution provides a stringent test of our computer modeling method and serves as an excellent example for the complexity of the RF field polarization behavior. The calculation was also carried out on a three-dimensional multitissue human head model created by transforming the segmented images of a male cadaver from the National Library of Medicine's Visual Human Project into a 3D grid with a resolution of 2.0 × 2.0 × 2.5 mm in the x, y, and z dimensions, respectively (26). The total cell number $N_x \times N_y \times N_z$ of the human head model was 310 × 162 × 178. The head model incorporates 18 different types of human head tissues with corresponding electric properties (σ, ϵ_r) at 300 MHz (27).

Experimental Data Acquisition

All images were acquired on a 7.0 T whole-body imaging system (Magnex magnet with Varian NMR console) with TR/TE =1000/5 ms, matrix = 128 × 128, FOV = 20 × 20 cm, and slice thickness = 3 mm. The coil input power level for maximum global FID intensity was determined to produce a nominal 90° flip angle. The head gradient echo (GE) images were also acquired from a normal volunteer with the head placed so that the occipital lobe was roughly coaxial with the coil and the back of the head was 1.5 cm from the coil center.

Computer Calculation

All numerical simulations were performed on a personal computer with the XFDTD program (REMCOM, State College, PA), which used the finite difference time domain (FDTD) method to solve Maxwell's wave equations (28,29). Using the RF field numerical solution, the signal intensity distribution of a gradient-echo image was calculated in the following three steps (8,13,26,30,31). Since all calculations are performed for sinusoidal steady-state fields, complex phasor notation, denoted with a circumflex, is used to represent the RF field variables in the following discussion.

Calculation of Transmission Field $\hat{\boldsymbol{B}}_t$ and Magnetic Resonance Response

The nuclear spin precession is assumed to be in the positive, or counterclockwise, direction. To produce a quadrature transmission field $\hat{\mathbf{B}}_t$ rotating in this direction, the calculation is performed by assigning the phase of the driving voltage source in coil A $\phi_A = 0°$ and in coil B $\phi_B = 90°$. Since only the positive circularly polarized component of the transmitting field $\hat{\mathbf{B}}_t$ contributes to the excitation of the spins, the RF field must be decomposed into two rotating fields: the positive circularly polarized component $\hat{B}_t^+$, which rotates in the direction of nuclear magnetic moment precession (counterclockwise direction), and the negative circularly polarized component $\hat{B}_t^-$, which rotates opposite to the direction of precession (clockwise direction)

$$\hat{B}_t^+ = \frac{\hat{B}_{tx} + i\hat{B}_{ty}}{2} \quad [1]$$

$$\hat{B}_t^- = \frac{\hat{B}^*_{tx} + i\hat{B}^*_{ty}}{2} \quad [2]$$

where $\hat{B}_{tx}$ and $\hat{B}_{ty}$ denote the x and y components of $\hat{\mathbf{B}}_t$, respectively, and the asterisk denotes a complex conjugate operation.

Ignoring the effects of relaxation and susceptibility on the response to simplify the problem, the magnitude of the transverse nuclear magnetization in a GE sequence with a rectangular RF pulse is given by (26, 31)

$$M = M_0 \sin(\gamma\tau|\hat{B}_t^+|V) \quad [3]$$

where γ is the magnetogyric ratio, τ is the pulse duration of the transmission field, V is a dimensionless constant that can be seen as proportional to the coil driving voltage, and M_0 is the initial magnetization. The absolute value of the polarization component $|\hat{B}_t^+|$ is given by

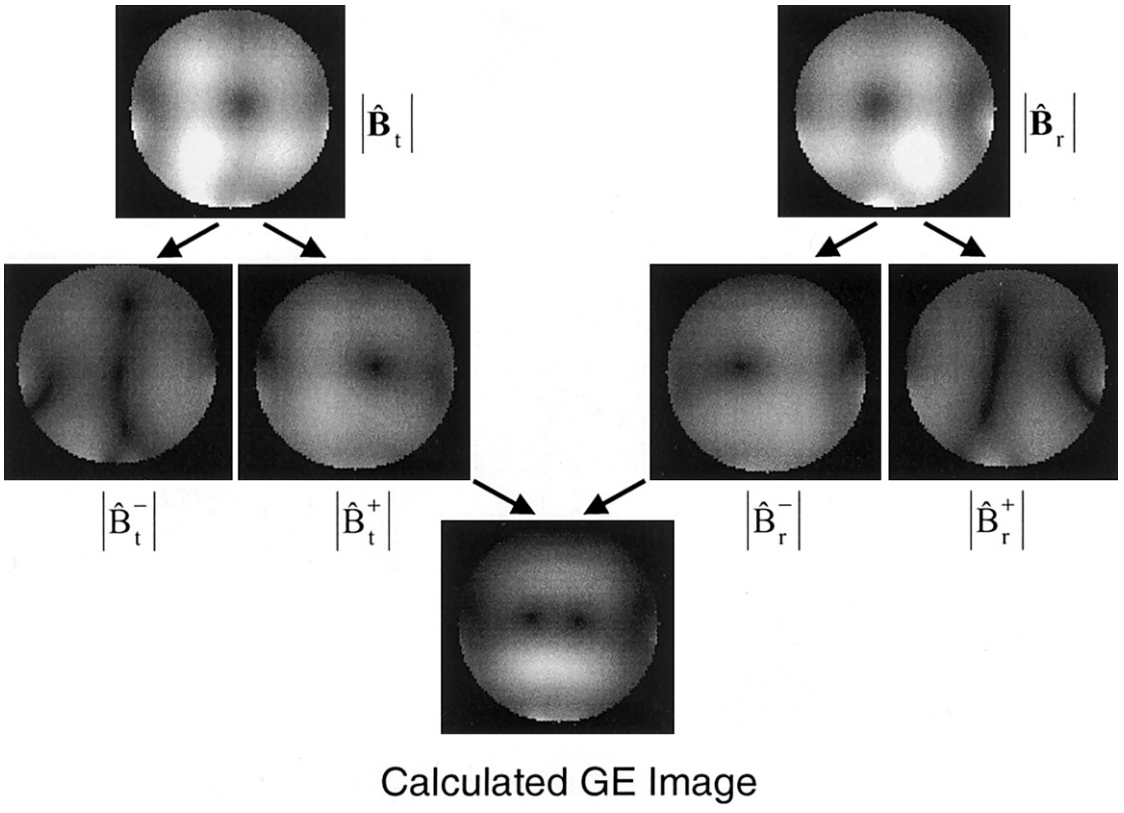

FIG. 2. The magnitude of the RF fields and their circularly polarized components in the axial plane for each step in calculating the gradient echo image of a saline phantom ($\sigma = 0.26$, $\epsilon_r = 78$). The calculated image from this sample exhibits a characteristic signal intensity pattern.

$$|\hat{B}_t^+| = ([\mathrm{Re}(\hat{B}_t^+)]^2 + [\mathrm{Im}(\hat{B}_t^+)]^2)^{1/2} \quad [4]$$

where $\mathrm{Re}(\hat{B}_t^+)$ and $\mathrm{Im}(\hat{B}_t^+)$ are the real and imaginary parts of $\hat{B}_t^+$.

Calculation of Reception Field $\hat{\boldsymbol{B}}_r$

The current in the receiving coil is induced by the precessing magnetic moments. For quadrature reception, the field caused from reception coil is calculated by assigning the phase of driving voltage source $\phi_A = 90°$ in coil A and $\phi_B = 0°$ in coil B, respectively. Then the reception field $\hat{\mathbf{B}}_r$ in xy plane is decomposed into two circularly polarized components as $\hat{B}_r^+$ and $\hat{B}_r^-$ in the same fashion as for the transmission field. Following the principle of reciprocity, the reception distribution is proportional to (30):

$$|\hat{B}_r^{-*}| = ([\mathrm{Re}(\hat{B}_r^{-*})]^2 + [\mathrm{Im}(\hat{B}_r^{-*})]^2)^{1/2}. \quad [5]$$

Calculation of the Signal Intensity Distribution

The product of the contributions of transmission and reception, then, yields the GE image intensity distribution

$$\mathrm{SI} = i\omega M_0 \sin(\gamma\tau|\hat{B}_t^+|V)(|\hat{B}_t^{-*}|). \quad [6]$$

In these calculations, M_0 is treated as proportional to water content.

In summary, to evaluate the image intensity distribution of a quadrature coil and sample configuration, the transmission field and reception field must be calculated separately. The quadrature transmission field rotates in the same direction as magnetization precession, while the reception field rotates in the opposite direction. Subsequently, each calculated field is decomposed into two circularly polarized components and only the circularly polarized components $\hat{B}_t^+$ and $\hat{B}_r^-$ contribute to signal intensity.

RESULTS

Figure 2 illustrates and summarizes the calculation procedure for a gradient-echo image calculated from the RF field numerical solutions. The transmission and reception fields are decomposed into positive and negative circularly polarized fields according to Eqs. [1], [2], [4], and [5]. The intensity distributions of the transmission and reception fields and their component fields are all distinctively different. $\hat{B}_t^+$ and $\hat{B}_t^-$ are no longer mirror images of each other as in the linear surface coil case (12), and the overall intensity of $\hat{B}_t^+$ is significantly stronger than $\hat{B}_t^-$. For the reception field, the overall strength of $\hat{B}_r^-$ is stronger than that of $\hat{B}_r^+$. This is expected because the quadrature coil increases the circularly polarized components $\hat{B}_t^+$ and $\hat{B}_r^-$. The unique signal intensity distribution can only be cor-

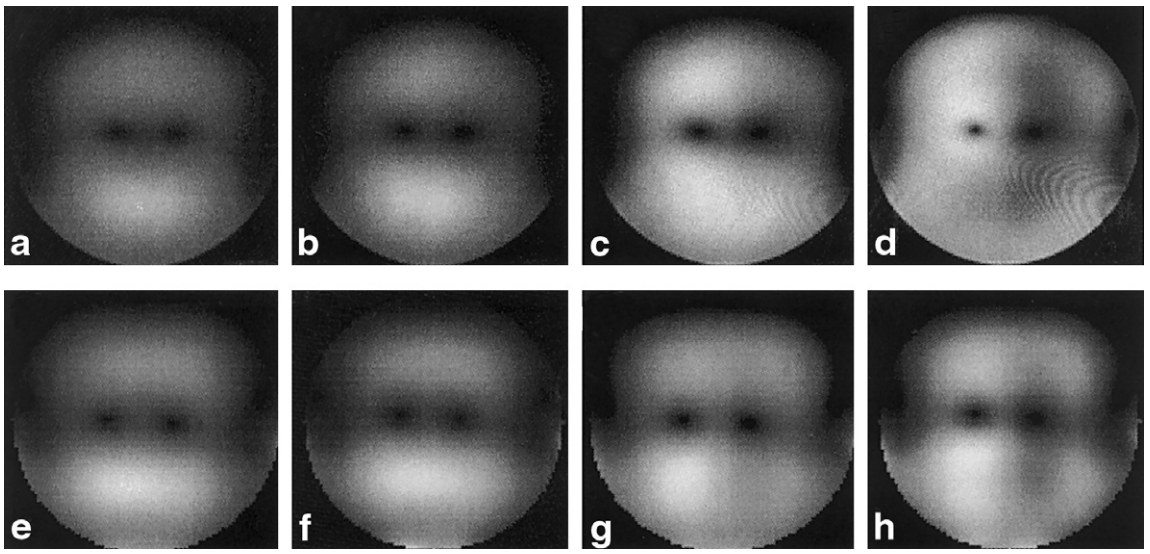

FIG. 3. The GE experimental (**a–d**) and calculated (**e–h**) axial image using the quadrature surface coil with different transmission power levels. There is a 6-dB power increment for each subsequent column of images from left to right. The specific experimental signal intensity patterns are reproduced by the calculated images. The signal intensity distribution becomes more asymmetric about the vertical centerline of the sample as the transmission power level increases.

rectly derived from Eq. [6] using the circularly polarized components $\hat{B}_t^+$ and $\hat{B}_r^-$. It is apparent that there is mirror symmetry about the vertical centerline between the transmission field $\hat{B}_t^+$ and reception field $\hat{B}_r^-$. Due to this symmetry in field intensity, the right and left "dark holes" seen in the calculated GE image in Fig. 2 originate from the contributions of $\hat{B}_t^+$ and $\hat{B}_r^-$, respectively.

To validate the computer modeling method, the calculated images are compared with the experimental results under the same conditions. Figure 3 shows four experimental and calculated axial GE images with 6 dB increments in the transmission power level. The nominal flip angles for the four images on both top and bottom rows are 11°, 22°, 45°, and 90°, respectively. The flip angles for the calculated images were obtained by adjusting parameter V in Eq. [3] to match the experimental image intensity distribution with 90° flip angle. Then, this value was divided by 2 for each successive calculated image with decreasing flip angle. The calculated images reproduce the experimental data in all relative power levels. Some subtle features such as the two "dark holes" near the center of the phantom in the images are exactly reproduced in the calculated images. For small flip angle images (Fig. 3a,e), the intensity distributions are approximately symmetric about the centerline of the coil and phantom. With increasing flip angle, the symmetry in the signal intensity pattern disappears. This behavior is mainly caused by the asymmetry in transmission and reception in the data acquisition process. As seen in Eq. [6], transmission is proportional to $\sin(\gamma\tau|\hat{B}_t^+|V)$, while reception is directly proportional to $|\hat{B}_r^-{}^*|$. The signal intensity is approximately proportional to $|\hat{B}_t^+| \times |\hat{B}_r^-{}^*|$ when the flip angle is small. Since the distributions of $|\hat{B}_t^+|$ and $|\hat{B}_r^-{}^*|$ are mirror images of one another, the resultant images are symmetric. The asymmetry becomes apparent when the small angle approximation is no longer valid due to an increase in transmission power or stronger transmission field in certain local areas. As a result, the asymmetry is more visible in the region of the phantom near the coil where the $\mathbf{B}_1$ field is relatively strong.

With this numerical method, the manifestation of the wave behavior in signal intensity distributions in images of the human head image intensity can be analyzed. Figure 4 shows the human head images acquired with the quadra-

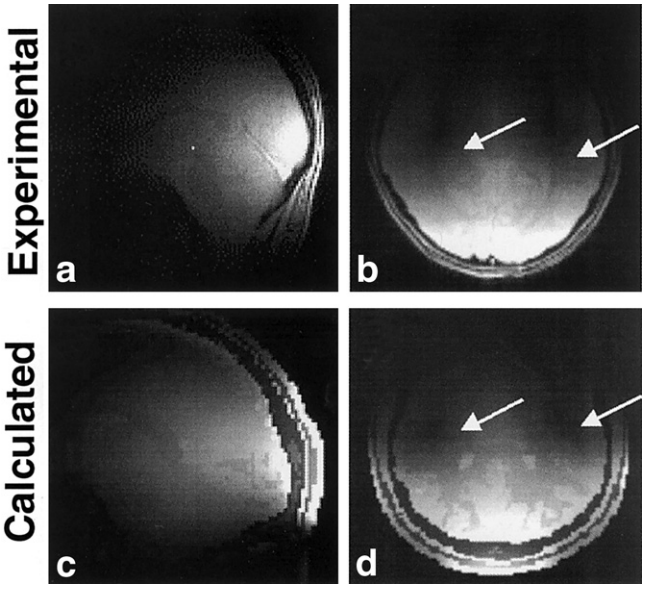

FIG. 4. The experimental sagittal (**a**) and axial (**b**) GE images acquired with a quadrature surface coil at 7.0 T and calculated images (**c,d**) of the corresponding planes from the numerical B_1 field solutions. The dark bands on each side of head (arrows) in the images can be seen in the calculated images.

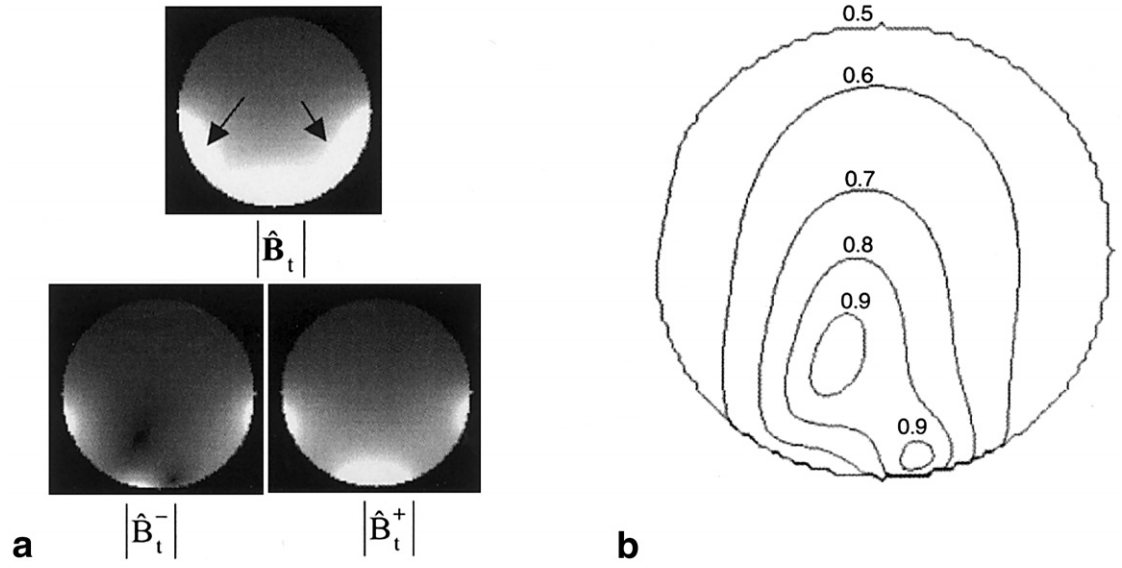

FIG. 5. The gray scale plots of the transmission field and its circularly polarized components (**a**), and the contour plot of β_t (**b**) of the quadrature surface coil in free space ($\sigma = 0$, $\epsilon_r = 1$). The plot for $|\hat{\mathbf{B}}_t|$ shows the field strength distribution while $|\hat{B}_t^+|$ and $|\hat{B}_t^-|$ depict the positive and negative circularly polarized components of the transmission field. The β_t contour plot describes the polarization distribution of RF field without the implication of the spatial field strength variation.

ture surface coil at 7.0 T, along with the corresponding calculated images. The experimental and calculated images show similar distributions in signal intensity. In particular, a nonanatomical feature of two vertical dark bands (arrows) on each side of the head seen in the experimental axial image is reproduced in the calculated image. The formation of such an intricate intensity distribution can be understood by examining the quadrature fields and their circularly polarized components in the following discussion and Fig. 5. The overall signal intensity decrease in the posterior–anterior direction arises from amplitude attenuation of the RF field of the surface coil.

To evaluate the effective circularly polarized component generated by a quadrature coil, a polarization ratio of the transmission field can be defined as

$$\beta_t \equiv \frac{|\hat{B}_t^+|}{(|\hat{B}_t^+| + |\hat{B}_t^-|)}. \quad [7]$$

Using this quantity, the spatial distribution of the polarization can be delineated from that of the corresponding field magnitude. For example, the polarization is circular if $\beta_t = 1$, linear if $\beta_t = 0.5$, and elliptical if $1 > \beta_t > 0.5$. For the case of $0 < \beta_t < 0.5$, the RF field is also elliptically polarized but with its major component rotating opposite to that of the quadrature field by the coil. Similarly, the polarization ratio for reception, β_r, can be defined and discussed.

Figure 5a shows the magnitudes of the calculated transmission field $|\hat{\mathbf{B}}_t|$ and its circularly polarized components $|\hat{B}_t^+|$ and $|\hat{B}_t^-|$, in the center transverse plane of a surface quadrature coil for $\epsilon_r = 1$ and $\sigma = 0$ (free space) at 300 MHz. Without a high permittivity load, the wave behavior is insignificant. The field distributions are similar to expectations for the quasistatic case and approximately symmetric with respect to the coil's center axis. The slight asymmetry in the field distribution can be attributed to the asymmetric geometry of the coil configuration. The magnitude of the field $\hat{\mathbf{B}}_t$ is strong in the region near the surface coil and falls off rapidly. $|\hat{B}_t^+|$ appears stronger than $|\hat{B}_t^-|$ in an extended area. For a quadrature coil during transmission, $\hat{B}_t^+$ is the major component, while $\hat{B}_t^-$ can be regarded as a residual field that is not used in inducing a flip angle. Where $|\hat{B}_t^-|$ is weaker than $|\hat{B}_t^+|$, the field is predominantly circularly polarized in the proper direction for transmission. For example, both $|\hat{B}_t^+|$ and $|\hat{B}_t^-|$ fields are strong in the areas (arrows) in Fig. 5 contributed dominantly from either coils A or B. In these regions the RF field is strong in magnitude but has poor circular polarization and is nearly linearly polarized. The dark regions in $|\hat{B}_t^-|$ field in the lower medial region indicate that the field is predominantly circularly polarized in the positive direction. This can be seen more quantitatively in the β_t contour plot in Fig. 5b as the 0.9 contours coincide with the dark regions in the $|\hat{B}_t^-|$ magnitude. Since the distributions in polarization ratio and magnitude of the RF field are complementary, the unloaded coil produces a desirable large uniform $|\hat{B}_t^+|$ region. In addition, since $\beta_t \geq 0.5$ within the sample region, the RF field is either linearly or circularly polarized in the positive direction. Thus, this coil would be expected to produce a better performance than a linear coil with similar geometry and a load at low fields where the wave behavior is not significant.

Figure 6 shows field plots inside the head model in the same fashion as in Fig. 5. The RF field appears to penetrate deeper than that without a load as a result of the high permittivity of the sample (32,33). The field distributions become less homogeneous and asymmetric. Most strik-

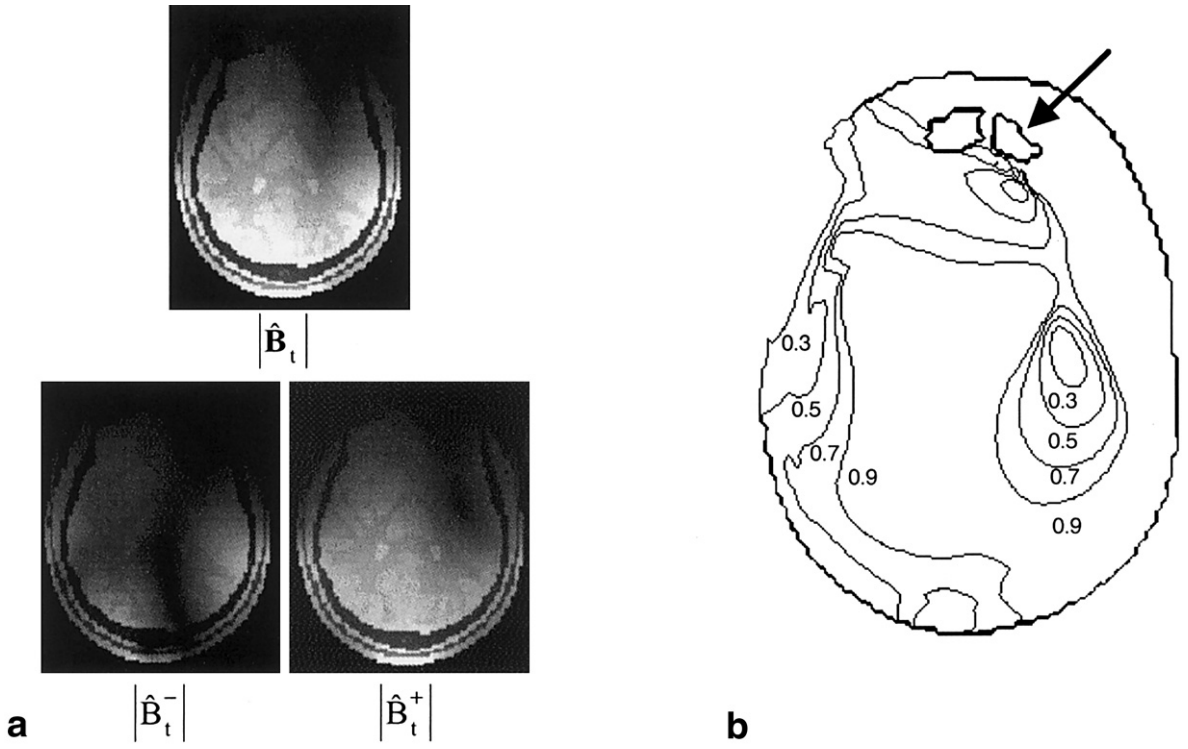

FIG. 6. The magnitude of the transmission field and its circularly polarized components of the quadrature surface coil (**a**) are significantly different in a human head than in free space (Fig. 5). The corresponding contour plot β_t (**b**) reveals the drastic changes in polarization as the RF field in some areas is polarized in the opposite sense than the quadrature coil ($\beta_t < 0.5$). The two frontal regions pointed to by the arrow are the image voids of the frontal sinus in the head model.

ingly, there are some areas where $\beta_t < 0.5$, indicating that the RF field is predominantly polarized in the negative direction of quadrature field of the unloaded coil. Introducing a high-permittivity sample alters not only the RF field strength but also the polarization distribution. As a result, the uneven signal intensity distribution can be caused by variations in both magnitude and polarization distributions associated with the wave behavior. This finding is important because it significantly challenges the basic approach in coil design for creation of a circularly polarized field in a region of interest for high field imaging. In our case, the quadrature coil design optimized in free space produces a less desirable signal intensity distribution in the human head. The right and left dark bands in the axial image of the human head in Fig. 4 are apparently caused by the reversed polarization in these regions in $|\hat{B}_t^+|$ and $|\hat{B}_r^-|$, respectively. The polarization of the RF fields in these surrounding areas changes drastically from one direction to the other. The close resemblance in intensity distributions between experimental and calculated images in Fig. 4 demonstrates that such changes in RF field polarization indeed exist in the human head.

DISCUSSION

Accurate prediction of experimental results by numerical methods confirms that our numerical method correctly simulates the electromagnetic interactions between the coil and sample in the process of image acquisition using a quadrature coil. As shown in Fig. 2, the transmission and reception fields are two distinct fields. One is produced by the input current in the coil and the other by the current induced by the transverse magnetization. The latter is used when the principle of reciprocity is applied for evaluation of the reception distribution. For a linear coil used during both transmission and reception, the spatial distribution of $\hat{\mathbf{B}}_r$ during reception is the same as that of $\hat{\mathbf{B}}_t$ during transmission, apart from a 180° global phase difference. The two circularly polarized components can be decomposed from the same field solution (12,14). Thus, $|\hat{B}_t^-|$ can be use to replace $|\hat{B}_r^-|$ in the evaluation of image intensity for the linear transmission and reception coil to avoid repeating the calculation. For a quadrature coil, a preferential direction of polarization is introduced which requires fixed phase relationships between the currents in the two orthogonal coils during excitation and reception, respectively. The intensity and polarization distributions of the transmission and reception fields are clearly different in this case and must be calculated separately. The difference between the transmission and reception fields is conceptually important even though the effect on image intensity distribution may be apparent in high-field human head images. In fact, it is necessary to use this approach to interpret the signal intensity distributions of a 50-cm radius cylindrical lossy dielectric phantom by a quadrature body coil at 1.5 T (13). In these cases, the wave behavior becomes significant because the dimensions of the samples are comparable to the RF field wavelengths of corre-

sponding static magnetic field strengths. Notice that there are mirror symmetries about the central vertical line between $|\hat{B}_t^+|$ and $|\hat{B}_r^-|$, and $|\hat{B}_t^-|$ and $|\hat{B}_r^+|$, apart from some subtleties due to the slight asymmetric geometric configuration of coils A and B (Fig. 2). These symmetries in field distributions vanish when the sample-coil configuration becomes asymmetric. Therefore, in general, it is necessary to calculate the transmission and reception field distributions separately for quadrature coils. With this numerical method, the experimental signal intensity distributions of phantoms with variable saline concentrations are reproduced precisely using an identical coil and sample computer model.

Since the RF field is elliptically polarized in samples with high permittivities, the performance of a quadrature coil design should be assessed by β_t and β_r in a given ROI in conjunction with the magnitude distribution. An optimal coil should produce a field with β_t and β_r greater than 0.5, in addition to strong B_1 magnitude distributions in a given sample. As demonstrated in Figs. 5 and 6, the value of β_t and the $\hat{\mathbf{B}}_t$ magnitude distributions are strongly dependent on sample geometry and the electric properties of the sample with given RF field frequency. Thus, an optimization of a quadrature coil design must be field strength- and sample-specific (10).

The precise reproduction of the complex pattern in the experimental images demonstrates the capability of our computer simulation method in analyzing multiple phase and multiple coil configurations at high frequencies. It is important to implement the multiple coil technologies in higher field systems. Besides the benefits that have been demonstrated at relatively low field strengths, multiple coil systems may offer an effective way to reduce the uneven image intensity artifacts. Our computer simulation method can be used to provide valuable information for RF field engineering in ultrahigh-field MRI.

CONCLUSIONS

A computer-aided method for analyzing the image intensity distribution using RF field solutions from a quadrature coil was developed and validated experimentally at 7.0 T. The complicated experimental image intensity distributions in a saline phantom at various transmission power levels are precisely reproduced by the numerical calculation method at 300 MHz. Thus, the method provides a reliable tool that can be very valuable for RF field engineering at high fields.

The transmission and reception fields are two physically different fields and must be calculated separately for producing the image intensity distributions. The exception for this is linearly driven simultaneous transmission and reception coils in which $\hat{\mathbf{B}}_t$ and $\hat{\mathbf{B}}_t$ are equal so $|\hat{B}_t^-|$ can be use to replace $|\hat{B}_r^-|$ (12).

The electrical properties and size of the sample strongly affect the RF field distribution in magnitude as well as polarization at high field strengths. The polarization of the RF field inside the sample varies drastically such that the RF field in certain regions can rotate predominantly in the direction opposite to the direction intended in driving the coil. Coil design optimization must be carried out with a proper load at an appropriate frequency and judged by the coil's performance in both field strength and polarization ratio distributions.

REFERENCES

1. Wen H, Jaffer FA, Denison TJ, Duewell S, Chesnick AS, Balaban RS. The evaluation of dielectric resonators containing H_2O or D_2O as RF coils for high-field MR imaging and spectroscopy. J Magn Reson 1996(Series B);110:117–123.
2. Han Y, Wright SM. Analysis of RF penetration effects in MRI using finite-difference time-domain method. In: Proc 12th Annual Meeting SMRM, New York, 1993. p 1327.
3. Carlson JW. Radiofrequency field propagation in conductive NMR samples. J Magn Reson 1988;78:563–573.
4. Tofts PS. Standing waves in uniform water phantoms. J Magn Reson 1994(Series B);104:001–005.
5. Alsop DC, Connick TJ, Mizsei G. A spiral volume coil for improved RF field homogeneity at high static magnetic field strength. Magn Reson Med 1998;40:49–54.
6. Ibrahim TS, Lee R, Abduljalil AM, Baertlein BA, Robitaille PML. Dielectric resonances and B1 field inhomogeneity in UHFMRI: computational analysis and experimental findings. Magn Reson Imag 2001;19: 219–226.
7. Vaughan JT, Hetherington HP, Otu JO, Pan JW, Pohost GW. High frequency volume coils for clinical NMR imaging and spectroscopy. Magn Reson Med 1994;32:206–218.
8. Sled JG, Pike GB. Standing wave and RF penetration artifacts caused by elliptic geometry: an electrodynamics analysis. IEEE Trans Med Imag 1998;17:653–662.
9. Vaughan JT, Garwood M, Collins CM, Liu W, DelaBarre L, Adriany G, Anderson P, Merkle H, Goebel R, Smith MB, Ugurbil K. 7T vs. 4T: RF power, homogeneity, and signal-to-noise comparison in head images. Magn Reson Med 2001;46:24–30.
10. Bomsdorf H, Helzel T, Kunz D, Roschmann P, Tschendel O, Wieland J. Spectroscopy and imaging with a 4 Tesla whole-body MR system. NMR Biomed 1988;1:151–158.
11. Foo TK, Hayes C, Kang YW. Reduction of RF penetration effects in high field imaging. Magn Reson Med 1992;23:287–301.
12. Collins CM, Yang QX, Wang JH, Zhu X-H, Adriany G, Michaeli S, Vaughan JT, Zhang X, Liu H, Anderson P, Ugurbil K, Smith MB, Chen W. Different excitation and reception distributions with a single-loop transmit-receive surface coil near a head-sized spherical phantom at 300 MHz. Magn Reson Med 2002;47:1026–1028.
13. Glover GH, Hayes CE, Helc NJ, Edelstein WA, Mueller OM, Hart HR, Hardy CJ, Donnell MO, Barber WD. Comparison of linear and circular polarization for magnetic resonance imaging. J Magn Reson 1985;64: 255–270.
14. Yang QX, Wang JH, Collins CM, Smith MB, Zhang X, Liu H, Michaeli S, Zhu X-H, Adriany G, Vaughan JT, Anderson P, Ugurbil K, Chen W. Analysis of wave behavior in dielectric sample at high field. Magn Reson Med 2002:47:982–989.
15. Chen CN, Hoult DI, Sank VJ. Quadrature detection coil — a further $\sqrt{2}$ improvement in sensitivity, J Magn Reson 1983;54:324–327.
16. Molyneaux DA, Quershi AH. Quadrature coil system for simultaneous reception. IEEE Trans Magn 1993;29:2470–2472.
17. Molyneaux DA, Quershi AH. Flexible quadrature coil system for simultaneous reception of magnetic resonance signals. IEEE Trans Magn 1995;31:3590–3592.
18. Thulborn KR, Shen GX. An integrated head immobilization system and high-performance RF coil for fMRI of visual paradigms at 1.5 T. J Magn Reson 1999;139:26–34.
19. Nitatori T, Seki T, Hachiya J, Kassai Y. Fast MR imaging of abdomen: application of the QD body coil and low refocusing flip angle. Radiat Med 1995;13:285–289.
20. Stensgaard A. Planar quadrature coil design using shielded-loop resonators. J Magn Reson 1997;125:84–91.
21. Fayad ZA, Connick TJ, Axel L. An improved quadrature or phased-array coil for MR cardiac imaging. Magn Reson Med 1995;34:186–193.
22. Sodickson DK, Manning WJ. Simultaneous acquisition of spatial harmonics (SMASH): fast imaging with radiofrequency coil arrays. Magn Reson Med 1997;38:591–603.

23. Pruessmann KP, Weiger M, Scheidegger MB, Boesiger P. SENSE: sensitivity encoding for fast MRI. Magn Reson Med 1999;42:952–962.
24. Wang Y. Description of parallel imaging in MRI using multiple coils. Magn Reson Med 2000;44:495–499.
25. Alecci M, Collins CM, Smith MB, Jezzard P. Radio frequency magnetic field mapping of a 3 Tesla birdcage coil: experimental and theoretical dependence on sample properties. Magn Reson Med 2001;46:379–385.
26. Collins CM, Smith MB. Signal-to-noise ratio and absorbed power as functions of main magnetic field strength, and definition of "90°" RF pulse for the head in the birdcage coil. Magn Reson Med 2001;45:684–691.
27. Gabriel C. Compilation of the dielectric properties of body tissues at RF and microwave frequencies. Air Force materiel command, Brooks Air Force Base, Texas: AL/OE-TR-1996-0037; 1996.
28. Yee KS. Numerical solution of initial boundary value problems involving Maxwell equations in isotropic media. IEEE Trans Ant Propag 1966;14:302–307.
29. Kunz KS, Luebbers RJ. The finite difference time domain method for electromagnetics, Boca Raton, FL: CRC Press; 1993.
30. Hoult DI. The principle of reciprocity in signal strength calculations — a mathematical guide. Concepts Magn Reson 2000;4:173–187.
31. Hoult DI, Phil D. Sensitivity and power deposition in a high-field imaging experiment. J Magn Reson Imag 2000;12:46–67.
32. Yang QX, Li CS, Smith MB. The effect of sample loading on the radio frequency magnetic field distribution in high field: contributions of dielectric resonance. In: Proc 12th Annual Meeting SMRM, New York, 1993. p 1367.
33. Keltner JR, Carlson JW, Roos MS, Wong ST, Wong TL, Buddinger TF. Electromagnetic fields of surface coil in vivo NMR at high frequencies. Magn Reson Med 1991;22:467–480.